Eur. Phys. J. Plus (2020) 135:165
https://doi.org/10.1140/epjp/s13360-020-00155-8

THE EUROPEAN PHYSICAL JOURNAL PLUS

Regular Article

Experimental studies of clustering in light nuclei: ^{11,12,13,16}C

Daniele Dell'Aquila[1,2,a]

[1] Department of Experimental Physics, Ruđer Bošković Institute, Bijenička 54, 10000 Zagreb, Croatia
[2] Università degli Studi di Napoli Federico II & INFN-Sezione di Napoli, Napoli, Italy

Received: 15 September 2019 / Accepted: 18 November 2019 / Published online: 28 January 2020

Abstract Different, complementary, techniques are used to experimentally probe clustering aspects in several carbon isotopes: ^{11,12,13,16}C. Our approaches involve breakup reactions with radioactive cocktail beams (^{16}C), compound nucleus reactions and resonant scattering at low energies (^{11,13}C), and direct reactions with the detection of in-flight resonance decay fragments (^{12}C). In this paper, we discuss results of our experimental campaign: in ^{11}C, we unveil the existence of a new excited state, characterized by clustering nature, at an excitation energy of 9.36 MeV ($5/2^-$); the decay path of the Hoyle state in ^{12}C (7.654 MeV, 0^+) is investigated with unprecedented precision; we refine the spectroscopy of ^{13}C above the α-threshold supporting the possible appearance of the $K^\pi = 3/2^\pm$ molecular bands, based on the α+^{9}Be structure, previously discussed in the literature; in ^{16}C, we find evidence for ^{6}He–^{10}Be decays. Our findings have an impact on the understanding of clustering phenomena in light nuclear systems.

1 Introduction

Clustering phenomena characterize nuclear physics since its very beginning [1]. They consist in the grouping of nucleons into correlated sub-units that have the role of fundamental bricks for the clustered system. Over more than half of a century, α-conjugate systems, i.e., nuclei with $N = Z$ and an even number of protons and neutrons, such as ^{8}Be, ^{12}C, ^{16}O and ^{20}Ne, played a fundamental role in the development of clustering phenomena in light nuclei. In a pioneering work [2], Hafstad and Teller pointed out the existence of a correlation between the binding energy of α-conjugate systems and the number of possible bondings between their hypothetical α-centers. This evidence demonstrated, to some extent, the existence of preformed clustered structures in self-conjugate nuclei and built the foundations for the α-particle model of the atomic nucleus. The case of nuclei away from the β-stability is particularly remarkable, and it has been clearly proven that the presence of extra neutrons may play a glue-like effect stabilizing more extreme α-cluster structures by means of molecular-like bondings [3–5]. These concepts establish a close analogy with the molecular binding in atomic molecules, where the exchange of electrons allows the molecule to be bounded. In nuclear neutron-rich systems, the wave function of extra neutrons, the valence neutrons, can be delocalized around α-particle cores, forming π or σ orbitals [6–9]. The idea of

[a] e-mail: daniele.dellaquila@irb.hr

neutron-molecular orbitals has been successfully applied to beryllium neutron-rich nuclei, the so-called nuclear dimers, [5,10–13] and used to predict the properties of multi-center cluster structures [14]. Several theoretical and experimental efforts have been recently made to extend the systematics from dimers to nuclear molecules with more than 2 cores [6,15]. In this framework, investigating the formation of clusters and molecules in carbon isotopes is key to understand clustering phenomena in light systems and their evolution to heavier nuclei [16].

In this paper, I report on our recent experimental investigations aimed to study clustering aspects in carbon isotopes and their evolution with the neutron excess. To help in clarifying the aspects described above, we selected several isotopes of carbon including both neutron-rich and neutron-deficient nuclei. In detail, we studied the proton-rich ^{11}C by means of the ^{10}B(p,α)^{7}Be reaction at low bombarding energies, and we investigated the direct decay of the Hoyle state (7.654 MeV, 0^+) in the self-conjugate ^{12}C via the ^{14}N(d,α)^{12}C* reaction; we made an extensive review of all data sets published in the literature and concerning ^{9}Be+α reactions to refine the spectroscopy of ^{13}C, and we studied the possible formation and decay of high-lying ^{16}C states via breakup reactions induced by radioactive ion beams. Such a diverse set of techniques allows us to explore clustering aspects in light nuclear systems with a multi-method and complementary point of view. The paper is organized as follows: Sect. 2 reviews the state-of-the-art of the literature, Sect. 3 describes our experimental campaign and the corresponding data analysis, Sect. 4 discusses the impact of our results in the understanding of clustering phenomena in light nuclei, Sect. 5 contains a final summary of the paper.

2 Clustering in ^{11,12,13,16}C: state-of-the-art

Recent theoretical and experimental efforts have been mainly focused to investigate the role of extra neutrons in three-center nuclear systems [17–22]. The corresponding $N\alpha$ system, ^{12}C, is a crucial point to understand such molecular-like structures. The famous Ikeda diagram [23] suggests that the appearance of $N\alpha$ cluster configurations is enhanced in the proximity of the threshold energy. For example, the second excited state of ^{12}C (7.654 MeV, 0^+), $^{12}C_{0_2^+}$, very close to the 3α disintegration threshold ($\approx$ 7.275 MeV), has a well pronounced cluster configuration. For this state, a pioneering theoretical work based on the α-particle model has suggested a linear molecular configuration of 3α particles [24]. Recently, the experimental evidence for the 2^+ rotational excitation of such state has ruled out the linear chain hypothesis [25,26]. State-of-the-art theoretical calculations based on microscopic models succeed in describing this state as a weak mixture of configurations including weakly bounded triangular configurations and bent-arm arrangements of the 3α particles [27,28]. Because of its pronounced cluster nature, the $^{12}C_{0_2^+}$ state, also named as the Hoyle state in ^{12}C for its critical astrophysical consequences (see Ref. [29] and references therein), has been indicated as the ideal starting point to construct molecular-like configurations in carbon isotopes by adding extra neutrons [14]. The formation of linear chain structures consisting in 3α-particles and valence neutrons has been speculated. Such a peculiar structure could be possible only thanks to the extra stability given by valence neutrons, as similar structures in ^{12}C are unstable against the bending motion [6].

The first example of this systematics is the ^{13}C nucleus. Milin and von Oertzen [19] established a set of states candidate to form parity inversion doublets: $K^\pi = 3/2^\pm$, based on the ^{9}Be$(3/2^-, g.s.) + \alpha$ structure. The $K^\pi = 3/2^-$ band should be built on the 9.897 MeV state, while the $K^\pi = 3/2^+$ would have the 11.080 MeV as the band head. The resulting momenta

of inertia are compatible with a linear chain arrangement of the three α-particles bound by a covalent neutron. Excited states linked to the ^{9}Be($1/2^+$, 1.68 MeV) + α structure are also predicted. These states are associated to possible 3α triangular configurations. A doublet of $J^\pi = 1/2^\pm$ experimentally observed states lying, respectively, at 10.996 MeV and 8.86 MeV are considered as candidates for this structure. The distinction between the ^{13}C linear and triangular α-cluster arrangement is indicated to be linked to the two different valence neutron configurations of the underlying ^{9}Be nucleus, respectively, σ and π-orbitals in the molecular orbital approach. ^{13}C low-lying states have been also object of recent microscopic 3α-n calculations [30–33]. Furutachi and collaborators used the $3\alpha + n$ cluster model to predict high energy ^{13}C rotational bands, based on its 3α cluster structure [31]. Their model is able to reproduce the energy of the ground state of ^{13}C but not the energies of the $5/2^-_1$ and $7/2^-_1$ members of the ground state band. Two excited rotational bands are predicted to be built on $3/2^-_2$ (11.4 MeV) and $3/2^-_3$ (14.5 MeV) states around the threshold energy, called, respectively, $K^\pi = 3/2^-_2$ and $3/2^-_3$. Both bands appear as characterized by large moment of inertia and a pronounced cluster configuration. The $K^\pi = 3/2^-_2$ band, which is linked by the authors to the $3/2^-$ band of [19], corresponds to a bent 3α linear chain configuration, more compact than the gas-like configurations predicted by the same model in the case of ^{12}C. A $1/2^-_2$ state is additionally found around the $3\alpha + n$ threshold (12.221 MeV), but it is not linked to the previously discussed rotational bands since it is not described by a $3\alpha + n$ structure. The existence of $1/2$ states in ^{13}C with a 3α nature is of noticeable interest as they are candidates for the Hoyle analogue state in ^{13}C. AMD calculations with the constraint of the harmonic oscillator quanta (HON) proved that, differently from the $1/2^-_2$ state predicted in [31], the $1/2^-_3$ ($E_x \approx 18.0$ MeV) has a strong $3\alpha + n$ structure, originating a large deformed rotational band ($K^\pi = 1/2^-$) [32]. The $1/2^+_1$ state identified at 14.9 MeV is associated to the $K^\pi = 1/2^+$ rotational band. It is suggested that the asymmetric intrinsic structure of ^{13}C might form a parity doublet $K = 1/2^\pm$ [32]. A $1/2^+_2$ state, lying at about 15.7 MeV excitation energy, is characterized by a large ^{12}C (0^+_2) $\otimes n(s_{1/2})$ spectroscopic factor. The authors of Ref. [32] interpret this state as the analogue of the $^{12}C_{0^+_2}$ state in ^{13}C. Another possible $^{12}C_{0^+_2}$ analogue state in ^{13}C is found, by means of $3\alpha + n$ OCM calculations [33], at an excitation energy of about 14.9 MeV. This state, indicated as $1/2^+_5$ in Ref. [33], can be described by a gas-like configuration with an extremely large radius (4.3 fm). It is characterized by a dominant (≈ 0.6) ^{12}C (0^+_2) $\otimes n(s_{1/2})$ spectroscopic factor [33].

The experimental situation concerning the spectroscopy of ^{13}C is still unclear. Recent α+^{9}Be resonant elastic scattering [34] are inconsistent with the systematics of [19]. Additionally, the spectroscopy of ^{13}C at excitation energies above the α emission threshold contains several contrasting J^π assignments [35], making it currently impossible to draw any firm conclusions on the theoretical aspects described above.

Another particularly interesting case is the neutron-rich ^{16}C nucleus. Molecular-like configurations in this nucleus might be constituted by a symmetric three-center structure of the type $3\alpha + 4n$. Calculations using the molecular orbital model have pointed out this structure as the most promising candidate for a linear chain configuration, where the 4 valence neutrons might give the necessary stability against the bending motion [6]. Refined theoretical calculations performed with the AMD code have been recently published [36], speculating the possible formation of an isosceles triangular configuration of 3α-particles with valence neutrons in the *sd* shell or a linear chain. The latter is qualitatively understood in terms of $3/2^-_\pi$ and $1/2^-_\sigma$ molecular orbits. This finding is in agreement with the prediction of the molecular orbital model [6]. In both cases, the valence neutrons are indicated to play a fundamental role to stabilize the structure. The formation of rotational bands is also studied in

Ref. [36]. Triangular and linear rotational bands are here found to be built, respectively, on the 8.0 MeV and 15.5 MeV states. Experimentally, the spectroscopy of ^{16}C is extremely poor [37]. Because of the limited availability of ^{16}C beams and the limited beam intensity, only a few and low statistics experiments are reported in the literature [38,39] and results are inconclusive with respect to the proposed rotational bands.

It is also interesting to investigate clustering aspects in the proton-rich ^{11}C nucleus. Its structure is intimately connected to that of its mirror nucleus ^{11}B. The latter, being an intermediate nucleus between the two-center beryllium isotopes and the three-center carbon ones, is considered a particularly challenging case study [40]. Additionally, the possible formation of diluted-gas states in ^{11}C and ^{11}B was recently conjectured by Kanada within the AMD framework [41]. In ^{11}C, the $3/2^-_3$ state, at an excitation energy of 8.10 MeV, was linked to a Hoyle-like structure of 2α-particles and a ^{3}He weakly interacting [41]. In the mirror ^{11}B nucleus, a diluted-gas state at 8.56 MeV excitation energy is reported [42,43]. This has a correspondence with the $3/2^-_3$ state of ^{11}C, which also presents a diluted-gas structure. In Ref. [42], a detailed study of mirror states in ^{11}C and ^{11}B is reported. Decays from the 8.65, 9.85, 10.7 and 12.1 MeV states in ^{11}C were clearly observed in Ref. [40] and linked to the $K = 3/2^+$ and $K = 5/2^+$ rotational bands in ^{11}C. Despite the strong experimental effort to reveal cluster structures in ^{11}C, to date, several ambiguities still affect its spectroscopy above the α-threshold. This prevents from drawing a fully clear picture of the clustering nature of this nucleus, demanding for new investigations.

3 Experimental campaign and results

To investigate the clustering aspects discussed above, we have conducted an experimental campaign. We performed a series of 4 experiments to probe several carbon isotopes: ^{11,12,13,16}C above the cluster emission threshold. In this section, I discuss details, analysis and results of our experiments.

3.1 ^{11}C

The main goal of our investigation is to probe possible $2\alpha + {}^3$He cluster configurations at high excitation energies. Such structures have been proposed in the literature and linked to the formation of molecular bands [44]. We investigated the spectroscopy of ^{11}C above the α-threshold (7.544 MeV) by exploiting the compound nucleus reaction ^{10}B(p,α)^{7}Be (Q = 1.145 MeV), at 0.63–1.028 MeV bombarding energies, and the existing elastic scattering ^{10}B(p,p)^{10}B data published in the literature. Together with the ^{7}Be(α,α), ^{7}Be(α,γ), ^{10}B(p,γ), ^{10}B(p,p) and transfer reactions, the ^{10}B(p,α)^{7}Be is an extremely powerful tool to investigate the spectroscopy, such as Γ_α, Γ_p and Γ_γ partial widths, of the ^{11}C compound nucleus (see, e.g., [34,44,45]). This information is key to unveil the existence of molecular states [34,44]. In addition to the nuclear structure aspects, our investigation has a clear multi-disciplinary interest. In nuclear astrophysics, the ^{10}B(p,α)^{7}Be reaction is involved in the disintegration of boron in H-rich stellar environments [46]. An accurate knowledge of the ^{10}B(p,α)^{7}Be S-factor is crucial not only to describe the abundance of ^{10}B in the universe but also to constrain mixing phenomena occurring in such stars [47]. In applied physics research, a precise knowledge of the ^{10}B(p,α)^{7}Be integrated cross section is required to exploit proton-induced reactions for the development of new-generation a-neutronic fusion reactors for the production of clean energy [48,49].

The ^{10}B(p,α) reaction at low energy exhibits two different exit channels: ^{10}B(p,α_0)^{7}Be and ^{10}B(p,α_1)^{7}Be. In the first, the residual ^{7}Be nucleus is in its ground state, while, in the latter, the first 0.43 MeV state in ^{7}Be is populated. At low energy (e.g., $E_p < 1$ MeV), the Coulomb barrier strongly suppresses the α_1 channel with respect to the α_0 one [51]. For this reason, in this analysis we decided to focus exclusively on the ^{10}B(p,α_0)^{7}Be reaction. In the literature, quite poor data concerning the ^{10}B(p,α_0) reaction are reported. Recently, indirect methods such as the Trojan Horse Method (THM) have been used to investigate this reaction at extremely low energies [52–54]. Extrapolations of the ^{10}B(p,α_0) S-factor have been obtained down to zero-energy, relying on the existing higher energy data above 1 MeV bombarding energies. In this energy region, the cumulative α_0 and α_1 cross section has been measured by Jenkin et al ($E_p \approx$ 3–5.5 MeV) [55] and, more recently, by Kafkarkou et al ($E_p \approx 2-5.5$ MeV) [56]. At lower bombarding energies ($E_p \approx 0.5-2.0$ MeV), extremely limited data are reported in the literature. The only existing angle-integrated measurement is performed with the activation technique of boron samples [57]. Such a technique does not allow to disentangle the α_0 and α_1 channels. The data of Ref. [57] is affected by very large error bars (of the order of 20–30%). In the same energy region, the very old data of Ref. [58] ($E_p \approx$ 0.5–1.6 MeV) and Ref. [51] ($E_p \approx$ 0.8–1.7 MeV) are also reported. They have been obtained with very refined detection devices (a magnetic spectrometer and an electrostatic analyser, respectively). Both these old data sets don't allow to extract the integrated cross section: the first data set [58] reports the differential cross section (DCS) for α_0 and α_1 channels obtained only at one angle ($\theta_{cm} \approx 140°$), while, in the second data set [51] angular distributions are reported only for five bombarding energies, down to 1 MeV.

Our experiment was performed at the Laboratorio dell'Acceleratore (LdA) of the University of Naples "Federico II" [59–62]. A high-precision proton beam was delivered by the TTT3 tandem accelerator at an intensity of 1 nA, to reduce pile-up effects. The beam energy spread was estimated to be around 0.2%, and the diameter of beam spot on the target did not exceed 2 mm, as carefully described in Ref. [50]. We performed 40 keV step measurements in the proton energy range $E_p = 0.63$–1.028 MeV. A Faraday cup, connected to a digital current integrator, was used to integrate the beam intensity over each of the experiment runs. A circular scattering chamber, containing experiment target and detectors, was kept at a vacuum level of the order of 10^{-6} mbar for the whole duration of the experiment. The target was constituted by a Boron layer (38 μg/cm^2 nominal thickness, isotopically enriched in ^{10}B at 99.9% level) with a small quantity of polyvinyl formal ($C_3H_6O_2$, of the order some μg/cm^2) to ensure its mechanical stability. Its stoichiometric properties were monitored during the beam time by analyzing elastic scattering peaks. The high level of purity of our beam is crucial to disentangle the contribution of the ^{10}B(p,α_0) reaction from various contaminant contributions naturally present in similar targets. Such elements were carefully analyzed by means of a dedicated elastic backscattering study with of 0.988 MeV protons. At θ_{lab}=140° [50]. We evidence contributions of Li and Al, probably due to contaminants in the boron powder used to manufacture the target, C and O, due to the polyvinyl formal layer, Cu, due to the use of a copper mortar for the boron e-beam evaporation, and Cl and Ba are due to the use of the $BaCl_2$ release agent in the target manufacturing procedure. Taking into account these expected contaminant contributions, we have analyzed the corresponding kinematic curves of the light ejectile produced by reaction on contaminants induced by the proton beam. Results of this analysis, for $E_p = 950$ keV, as an example, are shown in Fig. 1 with lines of different colors corresponding to the various contaminant reactions indicated in the legend. The black line represents the kinematic curve for the α-particle of the ^{10}B(p,α_0), hereafter α_0. As clearly visible, the ejectile energy E_i of the α_0 group is well separated from other contaminant ejectiles for all forward angles $\theta_{LAB} < 90°$. The situation is much more

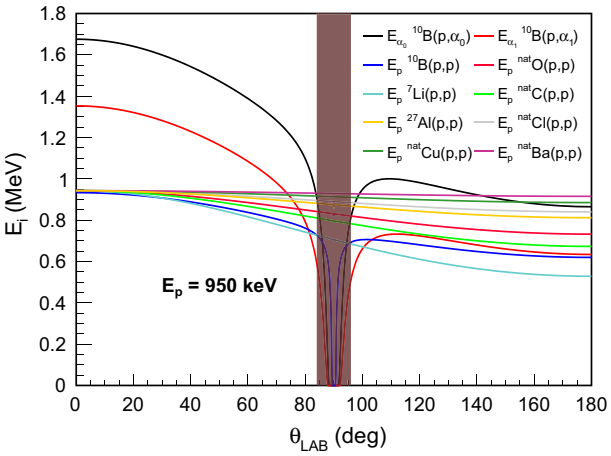

Fig. 1 E_i versus θ_{LAB} kinematic curves for the ^{10}B(p,α_0) reaction compared to the expected contaminant reactions, according to the analysis described in Ref. [50]. The brown band corresponds to the region shadowed by the target frame

complicated at backward angles, where we expect a strong overlap between the ^{10}B(p,α_0) reaction and the $^{\mathrm{nat}}$Ba,Cu,Cl(p,p_0) scattering products.

In order to overcome the limitations introduced by such a complicated kinematics, we designed the arrangement of detectors sketched in Fig. 2. The detection system consisted in 10 high-resolution ($\approx 0.3\%$) silicon detectors placed at 10 cm from the target and with an active surface (opportunely collimated) of 1×1 cm^2. Four detectors were placed at forward angles, $\theta_{\mathrm{LAB}} = 30°, 40°, 50°, 60°$, while three couples of symmetrically displaced detectors were positioned at backward angles, $\theta_{\mathrm{LAB}} = 120°, 140°, 160°$. The latter were shielded with a 3 μm aluminum foil on the one side of the beam-line and unshielded on the opposite side, as schematically shown in Fig. 2. For the considerations of Fig. 1, only the forward detectors have direct access to the α_0 yield; for the backward detectors, instead, the presence of contaminants from $^{\mathrm{nat}}$Ba,Cu,Cl(p,p_0) scatterings prevents an unambiguous extraction of the α_0 yield. To extract the α_0 yield, we implemented a novel procedure that we called *inverse absorber method*. The method can be described considering a pair (shielded and unshielded) of symmetrically arranged detectors. In the shielded detector, because of the presence of the aluminum foil, the α_0 ejectiles are stopped before reaching the active volume of the detectors, while the light ejectiles produced by the $^{\mathrm{nat}}$Ba,Cu,Cl(p,p_0) contaminant scatterings are detected after some energy degradation. The basic idea is to obtain the yield of the α_0 process by subtracting the shielded spectrum from the unshielded one after proper manipulation. In order to make comparable the pair of spectra, we have processed the unshielded spectrum with a Monte Carlo simulation of energy loss and straggling, to simulate the effect of the absorber. In the simulation, all the particles are treated as protons. Figure 3 shows an example for a beam energy $E_p = 0.988$ MeV and a detection angle $\theta_{\mathrm{lab}} = 160°$. The unshielded spectrum is the green one in figure. The blue spectrum is the shielded spectrum processed with our Monte Carlo simulation. The latter agrees in a satisfactory way with the shielded one, testifying that all the detected particles are protons. At an energy of about 700 keV, an extra yield is clearly present in the green spectrum, corresponding to the α_0 contribution not present in the shielded spectrum. The difference between the unshielded spectrum processed

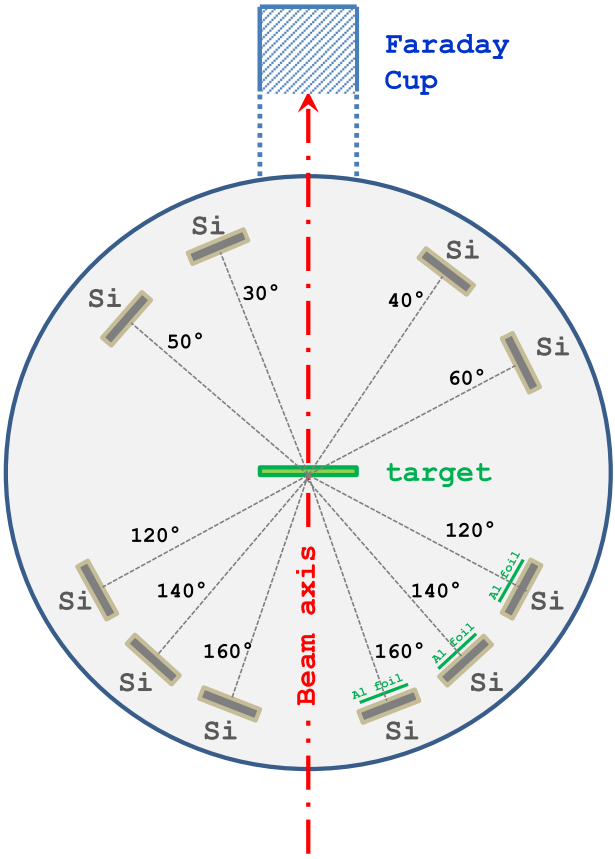

Fig. 2 A sketch of the vacuum chamber and detection setup used for the LdA experiment. The dash-dotted red line indicates the beam axis. 10 silicon detectors are placed at the two sides of the beam-line, covering the θ_{LAB} angles indicated in the figure. Three couples of identical detectors, shielded and unshielded, are placed at $\theta_{\mathrm{LAB}} = 120°$, 140° and 160° to implement the inverse absorber method described in the text

with the Monte Carlo simulation and the shielded spectrum corresponds to the red area and allows to unambiguously extract the yield of the α_0 process.

The differential cross section (DCS) of the ^{10}B(p,α_0)^{7}Be was estimated by using the measured experimental α_0 yields at various incident energies. The absolute units of the DCS are obtained by means of an internal normalization procedure to the ^{10}B(p,p_0) yield. The latter is measured at 140° and 160° and compared to the well-benchmarked data published in Refs. [63,64]. With this normalization procedure, we obtain the angular distribution in absolute units shown in Fig. 4 with the black points. At E_p lower than $\approx$ 0.785 MeV, some points at forward angles are missing, because of the overlap with the pile-up peak. As discussed in Ref. [50], it is interesting to observe that our angular distribution at $E_p = 1.010$ MeV agrees well with the one reported by [51] at similar energy (1 MeV). This testify the consistency of our method. It is important to stress that the angular distribution reported in Ref. [51] is the only one available in the literature in the $E_p \approx 0.5$–1.0 MeV domain.

To extract the angle-integrated cross section in absolute units, we used a Legendre polynomial fit procedure to the data of Fig. 4, as described in Ref. [50]. The resulting cross section

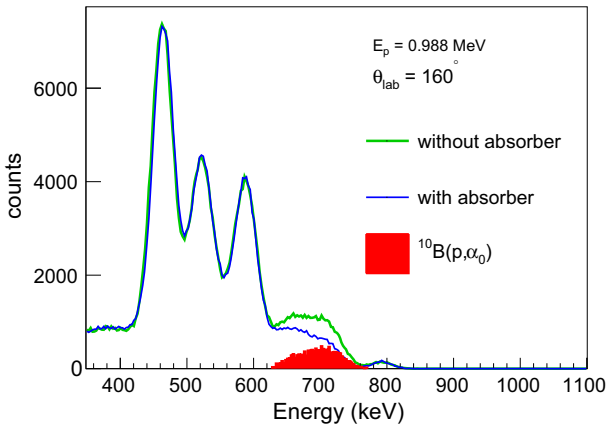

Fig. 3 The *inverse absorber method* applied, as an example, to the $E_{0.988}$ spectrum measured at $\theta_{\rm lab} = 160°$. The blue spectrum is obtained with the shielded detector, while the green one is obtained with an unshielded detector placed symmetrically with respect to the beam-line and processed by our Monte Carlo energy loss simulation. The red area corresponds to the extracted α_0 yield

is shown, as astrophysical S-factor (calculated as described in Ref. [65]), in Fig. 5a with full blue circles, as a function of the ^{11}C excitation energy. Error bars represent the statistical uncertainty on our measured data, arising from the statistical error associated to our Legendre polynomial fit. In this figure, for clarity, we do not report systematic uncertainties arising from the internal normalization procedure. Our data show a bump at ^{11}C excitation energy $E_x \approx 9.36$ MeV suggesting the possible presence of a new ^{11}C excited state not reported in the literature. The presence, for the first time, of fully reliable integrated cross section data points in the $E_x \approx 9$–11 MeV ^{11}C excitation energy region allows us to perform some more detailed analyses.

In order to refine the spectroscopy of ^{11}C in the $E_x \approx 9$–11 MeV energy region, we performed a comprehensive R-matrix fit of our data, together with the data reported in the literature and concerning ^{10}B(p,α_0)^{7}Be and elastic and inelastic scattering. The data sets used for our fit procedure are shown in the four panels of Fig. 5. For the ^{10}B(p,α_0)^{7}Be reaction (top panel), we complemented our new data set with the data reported in Refs. [51,58,66]. The data of Ref. [57], where the authors supply the sum of α_0 and α_1 channels and not the α_0 channel individually, have been excluded from our data set. The angular distributions reported by Cronin et al [51] in the $E_p = 1.0$–1.63 MeV domain point out small anisotropy effects ($\leq 10\%$). For this reason, in the absence of more detailed data, we decided, as a first approximation, to calculate the ^{10}B(p,α_0)^{7}Be angle-integrated cross section by using the α_0 angular distribution at $\theta_{\rm lab} = 90°$ reported in [51] (black triangles) and [66] (green stars) and assuming isotropy. We considered an additional indetermination of $\pm 10\%$ due to the isotropy assumption. The data by Brown et al [58] (DCS at $\theta_{\rm lab} \approx 137.8°$) were considered in the $E_p \approx 0.5$–1.2 MeV domain (open diamond in Fig. 5). Also in this case, we made an isotropic assumption to derive the corresponding angle-integrated cross section with an estimated indetermination of $\pm 10\%$. We normalized the data of Brown et al [58] to our data set introducing a common normalization factor of 0.76, to correct for possible normalization errors in Ref. [58]. With this normalization factor, the data of [58] agree well with our data. Elastic and inelastic scattering DCS data have been extracted from Refs. [63,64]. We considered the elastic scattering ^{10}B(p,p$_0$)^{10}B DCS at 130° and 150° (Fig. 5b, c) and the

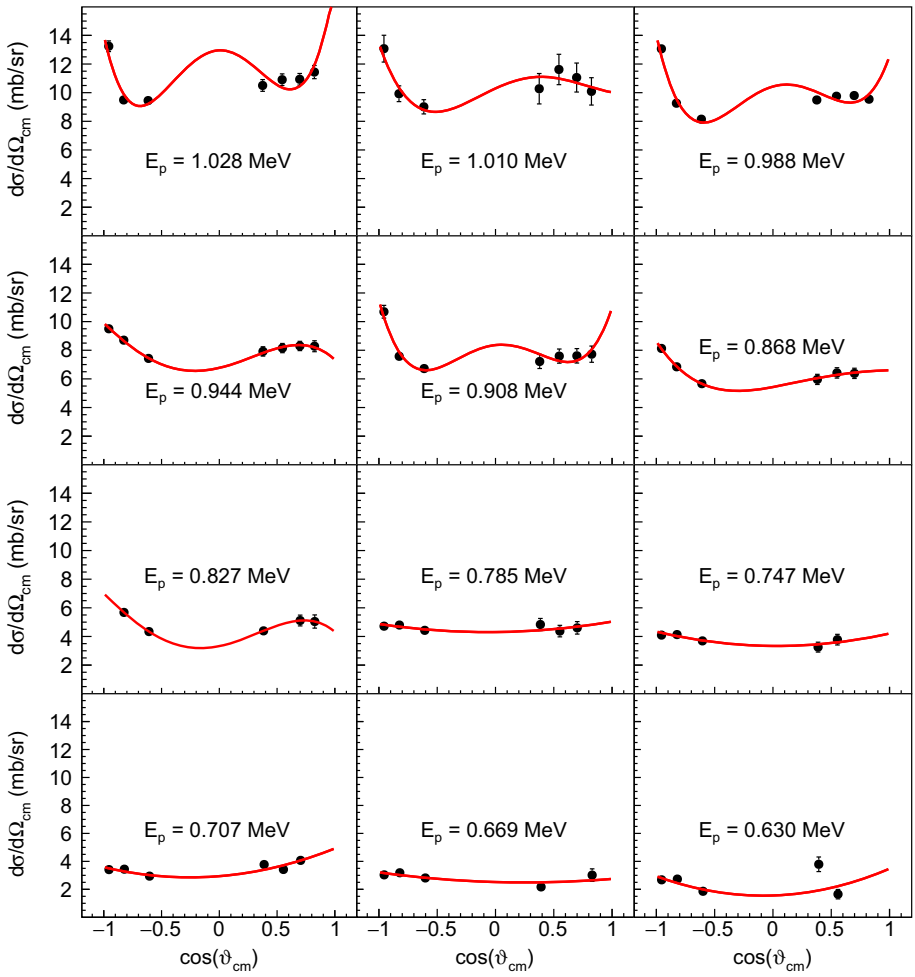

Fig. 4 ^{10}B(p,α_0)^{7}Be DCS angular distributions obtained in our work. The red line is the result of our comprehensive R-matrix fit of the data sets reported in Fig. 5

DCS data of the ^{10}B(p,α_1)^{7}Be$_{0.429}$ reaction at 90° (Fig. 5d). ^{10}B(p,p$_0$) elastic scattering data, published by Refs. [34,44], have not been considered in the global fit because of strong differences between them. To perform the R-matrix analysis of all these data sets, we used the R-matrix code AZURE2 [67,68]. The channel radii have been estimated with the formula $R = 1.4 \times (A_1^{1/3} + A_2^{1/3})$ fm [34]. In the fit procedure, we allow the overall normalization of the elastic scattering data by Refs. [63,64] to be varied within ±15%. As a starting point of our fit procedure, we considered the ^{11}C excited states at 8.699, 9.20, 9.65, 9.78, 9.97, 10.083, 10.67 MeV and the spectroscopic parameters published in Refs. [34,44,45,69,70]. The gray dashed line in Fig. 5a shows the result of the R-matrix by considering this initial set of parameters. It is clear that the result is not satisfactory and an additional effort has to be made to reproduce the experimental data, especially at lower energies ($E_x < 9.7$ MeV). Analogously, disagreements are also observed in the elastic and inelastic scattering data, not reported in the figure for clarity reasons. The excitation energies of states considered

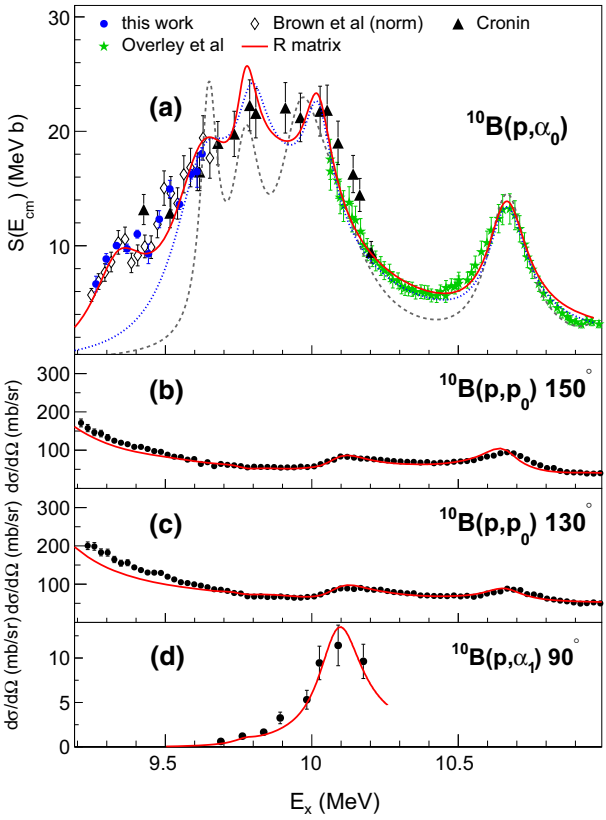

Fig. 5 **a** ^{10}B(p,α_0)^{7}Be angle-integrated cross section (blue points), compared to the data sets reported in the literature [51,58,66] and integrated with the procedure discussed in the text. **b**, **c** ^{10}B(p,p$_0$)^{10}B DCS at 130° and 150° from Refs. [63,64]. **d** ^{10}B(p,α_1)^{7}Be$_{0.429}$ DCS at 90° from Refs. [63,64]

in the fit, as well as their partial widths, were allowed to vary within reasonable limits, compatible with the indetermination quoted in the literature [69] and without overcoming the corresponding Wigner limit. The J^π assignments of the 9.65, 9.78, 9.97, 10.083, 10.67 MeV states were fixed to the values reported in the literature [34,44,45,69]. To account for the feature observed in Fig. 5a at about 9.36 MeV, we included an additional unreported ^{11}C state to the fit procedure, allowing its position to vary in the range $E_x = 9.3$–9.4 MeV. To simultaneously describe the resonant peak at about 10.1 MeV in the ^{10}B(p,α_1)^{7}Be$_{0.429}$ DCS and the broad bump at about 10.1 MeV in the elastic scattering DCS, we suggest to introduce a $5/2^+$ state at 10.1 MeV, having only Γ_{p0} and $\Gamma_{\alpha 1}$ partial widths. We obtain a very satisfactory reproduction of the experimental data by considering a J^π assignment $5/2^-$ for the 9.36 MeV. The red lines of Fig. 5 show the result of our fit procedure. Additionally, the consistency of the J^π assignment for the 9.36 MeV is also confirmed by the agreement between our measured ^{10}B(p,α_0) DCS angular distribution and the prediction of our fit (red lines in Fig. 4). The significant α decay width of the 9.36 MeV state (about 70% of the corresponding Wigner limit) suggests the possible α-cluster nature of this state. Finally, the blue dashed line in Fig. 5a is the result of the R-matrix calculation by using the spectroscopy parameters of the present analysis but without the 9.36 MeV state. It is clear that, without

including the 9.36 MeV state, the description of data is extremely poor at ^{11}C excitation energies lower than about 9.8 MeV. The spectroscopy of ^{11}C obtained in our analysis is reported in the Table 1 of Ref. [50].

3.2 ^{12}C

The Hoyle state in ^{12}C (7.654 MeV, 0^+) is a key system to understand clustering phenomena in light nuclei. Because of its pronounced 3α-cluster structure, its decay proceeds almost exclusively via α-particle emission, $\Gamma \approx \Gamma_\alpha$. Radiative decays, $\Gamma_{\rm rad}$ amount to only an extremely small fraction of the total decay width: $\Gamma_{\rm rad}/\Gamma_\alpha \approx 10^{-4}$. Additionally, two distinct decay paths are possible in the case of the α-decay: the so-called sequential (SD) and direct (DD) decays. In the first, an α-particle is emitted by leaving the residual ^{8}Be that subsequently decays into two α-particles. The DD corresponds instead to the instantaneous emission of 3α-particles, bypassing the intermediate formation of a ^{8}Be. A precise knowledge of the decay mechanism of the Hoyle state is particularly relevant to nuclear structure as well as to astrophysics. In nuclear structure, this information is crucial to models attempting to describe the cluster structure of light nuclei [27]. In the astrophysical domain, where the competition between the α-decay and the radiative decay affects the production of carbon in the universe, different α-decay paths might have strong consequences for the helium burning in massive stars [71]. In 1994, Freer and collaborators pointed out the dominance of the SD mechanism to the DD [72]. More recently, the publication of Ref. [73], showing evidence for a significant DD branching ratio, stimulated a series of higher resolution experiments to measure possible signals of DD. However, these recent results are often contrasting [71,74–76], making it currently difficult to draw a firm experimental conclusion regarding the possible existence of DD from the Hoyle state.

To address this fundamental problem, we have designed a high-selectivity and high-precision experiment using a new-generation hodoscope of silicon detectors called super-OSCAR [77–79]. This detector is a modified version of the OSCAR telescope [80] with 64 1×1 cm^2 individual silicon cells in a 8×8 configuration and without the additional strip detection stage described in Ref. [80]. The crucial advantage of a similar detector with respect to a conventional Double-Sided Silicon Strip Detector (DSSSD), used in previous high-resolution investigations of the Hoyle state, is the presence of independent detection cells. Previous works have indeed shown how the presence of misassigned tracks produced in DSSSDs artificially enhances signals of DD [76]. In our setup, the reconstructed particle tracks are unambiguous. Another crucial advantage of our study is the selectivity of the experiment. We use the ^{14}N$(d,\alpha)^{12}$C reaction induced by a 10.5 MeV deuteron beam to produce residual ^{12}C nuclei. They are tagged event-by-event by means of a backward detector ($\theta_{\rm LAB} = 125°$) capable to identify the emitted α from the ^{14}N$(d,\alpha)^{12}$C reaction. From the measurement of its momentum, we can infer emission direction and excitation energy of the residual ^{12}C. The superOSCAR hodoscope is placed in kinematical coincidence with the expected recoiling ^{12}C* in its Hoyle state to reconstruct its disintegration into 3α. The kinematical coincidence ensures the high selectivity of the experiment. To obtain a clear selection of the backward emitted α-particle, we use the technique of the anti-coincidence telescope previously discussed in [81]. This technique consists in the anti-coincidence between 2 detection stages of a telescope. To implement this technique, we used a silicon $\Delta E - E$ telescope, having a first detection stage (ΔE) with a thickness of 100 μm and a thick (1500 μm) detector as the second detection stage (E). With this configuration, particles coming from contaminant processes, such as (d,d) or (d,p) reactions on one of the target constituents, are enough energetic to punch-through the first detection stage and release a measurable signal

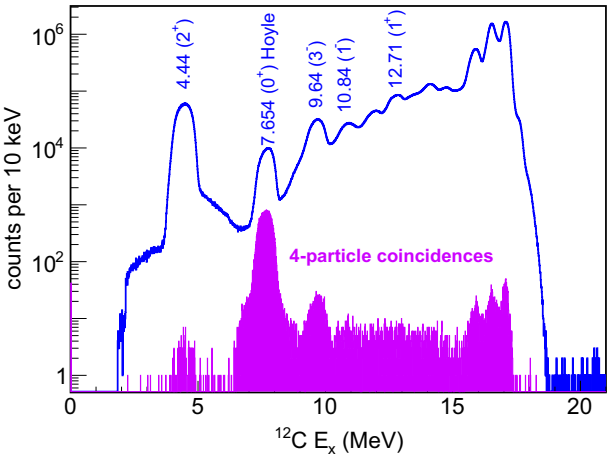

Fig. 6 ^{12}C excitation energy spectrum obtained from the measurement of the backward emitted particle with the anti-coincidence telescope, assuming that the particle is an α (blue spectrum). States in ^{12}C are indicated by labels. (purple histogram) as the blue histogram but requiring that 3 particles are detected by the forward hodoscope

in the second stage. This is not true for the α-particles emitted by ^{14}N(d,α) reactions that will be stopped in the first 100μm detection stage. The first can be ruled out by selecting signals in the first detection stage that are in anti-coincidence with the second detection stage. Additional details of this technique are discussed for example in [82].

Our experiment was carried out at the INFN-Laboratori Nazionali del Sud, exploiting the high-quality deuteron beams produced by the 15 MV tandem accelerator. We collected data along over 30 days of beam in order to maximize the statistics. We used a Melamine target $C_3H_6N_6$ to induce reactions on ^{14}N. To increase the stability of the target, it was deposed on a thin (15 μg/cm^2) carbon backing. The beam intensity was kept lower than 3 nA to minimize the pile-up. Figure 6 (blue line) shows the spectrum obtained with the first detection stage of the anti-coincidence telescope, assuming that the particle is an α, in terms of ^{12}C recoiling excitation energy. Several peaks are identified, corresponding to well-known states in ^{12}C that are indicated by labels in the spectrum, together with a background due mainly to α-emitting reactions on other components of the target. The latter affect exclusively the higher energy part of the spectrum and their contributions is in general well-separated by the Hoyle state peak identified in the figure. The blue spectrum of Fig. 6 collapses in the full purple one if one requires that 3-particles are detected by the forward hodoscope. In the latter, the ratio between the Hoyle state peak and the rest is drastically enhanced, testifying the high selectivity of the setup to Hoyle state decays. An extremely small fraction (less than 10^{-4} of the original area) of counts is visible under the 4.44 MeV peak. These are attributed mainly to pile-up events and spurious signals in the hodoscope. The background under the Hoyle state peak is strongly reduced by the 4-particle coincidence. The purple spectrum can be used to tag the Hoyle state production with high accuracy. If we perform such a selection, and assume that the 3 forward particles are α-particles, we can calculate the invariant mass of the 3α-particles. This is shown, in terms of ^{12}C excitation energy, if Fig. 7 with the purple points. A prominent peak is observed, it is centered at 7.654 MeV with the precision of less than 1 keV. This peak corresponds to well-identified Hoyle state decays, as testified by the result of a complete Monte Carlo simulation of our experiment (black dashed

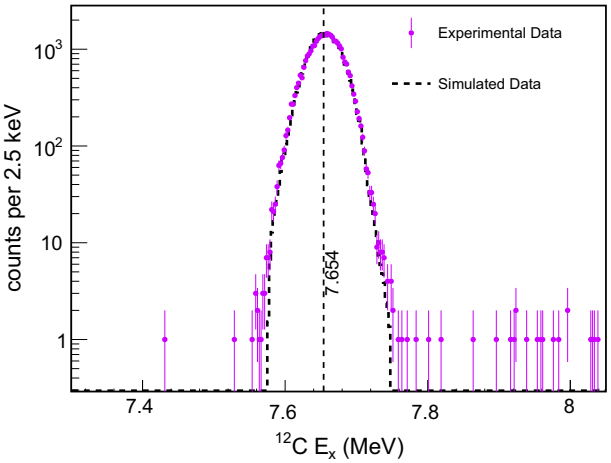

Fig. 7 ^{12}C excitation energy spectrum obtained from the invariant mass of the 3 particles detected by the forward hodoscope, assuming that they are α-particles, in coincidence with the backward emitted particle under the Hoyle state peak of Fig. 6

line). The small level of background, $\approx 0.036\%$ is attributed to a small fraction of pile-up and other contaminant events. This plot can be used to select Hoyle state events from the reaction ^{14}N(d,α)^{12}C* (7.654) by performing a narrow gate close to the center of the peak of Fig. 7.

To investigate the decay mode of the Hoyle state, we studied the topology of the 3α-particle emission in their phase space by using a procedure similar to the one adopted in Ref. [76]. We define the so-called radial projection (ε_i) of the symmetric Dalitz plot (see for example [71,83,84] and references therein). This is shown in Fig. 8 with the black points. In such a plot, one expects a peak corresponding to 0.506 in the case of a SD and an almost flat distribution between 0.33 (when particles share an equal amount of the decay energy) and 0.67 (when one α is emitted in the opposite direction of the other two) in the case of a DD uniformly in the phase space. In Fig. 8, we also plot, with a dashed line, the result of our detailed Monte Carlo simulation for a 100% SD scenario; in the latter we take into account reaction kinematics, beam spot size, the effect of the target and the detection process. It is clear that our Monte Carlo simulation quantitatively explains the trend of our data, except in the small tails. These can be attributed either to small signals of DD or to background events. The latter have indeed the same topology of DD and are therefore not distinguishable. Considering that all the counts that are quantitatively reproduced by our 100% SD simulation are well-identified SD and that the tails are background + DD signals, we can perform a statistical analysis of the recorded counts to establish the possible evidence of DD. We used the Feldman and Cousin's approach [85] for the analysis of small signals, assuming that both the DD and background counts are regulated by the Poisson statistics [86]. The lower limit of our DD finding is found to be compatible with *zero*. We conclude that DD signals are not statistically significant. We quote an upper limit on the branching ratio of the direct three α decay of 0.043% (95% C.L.). This value is about a factor 5 lower than the one found in the previous state-of-the-art experiment [76]. Our result provides important information about the α cluster structure of ^{12}C Hoyle state and can be useful to more effectively constrain theoretical models attempting to reproduce its structure.

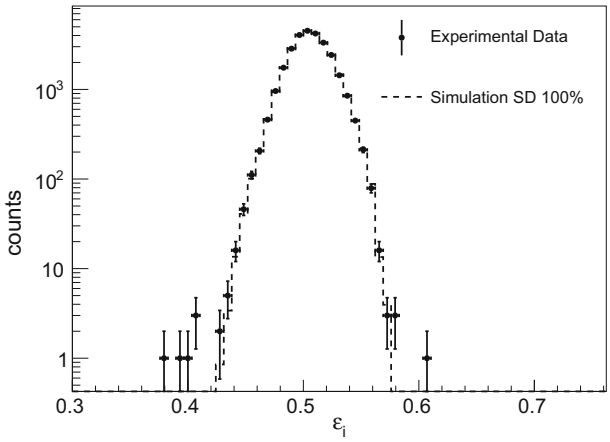

Fig. 8 Radial projection (ε_i) of the symmetric Dalitz plot for the 3α decay of the Hoyle state in ^{12}C. More details can be found in Ref. [83]

3.3 ^{13}C

To investigate the structure of ^{13}C above the particle emission threshold, a number of reactions have been indicated in the literature as particularly powerful tools: the α+^{9}Be elastic and inelastic resonant scattering [15,87–92], the ^{9}Be(α,n)^{12}C reactions [93–95], the n+^{12}C elastic and inelastic scattering [96–98], and transfer reactions such as the ^{9}Be(^{6}Li,d)^{13}C* case [99–101]. Among those, the α+^{9}Be scattering has been suggested as extremely selective to cluster states in ^{13}C because of the pronounced cluster nature of ^{9}Be [15]. Previous experiments tried to explore the structure of ^{13}C by means of the ^{9}Be(α,α)^{9}Be resonant elastic scattering. In Ref. [88], the authors investigate the ^{13}C excitation energy region $E_x \approx$ 13.3–14.5 MeV, with this reaction, by performing fits of experimental excitation functions at several angles with predictions based on the Blatt-Biedenharn formalism [102]. More recently, the authors of Ref. [15] measured the ^{9}Be(α,α)^{9}Be scattering at $\theta_{\rm CM} = 180°$ in inverse kinematics by using a helium gas target; results of this experiments were interpreted in terms of the R-matrix theory, successfully revising J^{π} assignments and the partial width values of several ^{13}C states in the $E_x \approx$ 13.3–16.2 MeV range. However, because of the limited angular and energy range of previous experiments, the spectroscopy of ^{13}C is still uncertain, e.g., there is no evidence for the $\frac{9}{2}^{\pm}$ members of the molecular bands suggested in Ref. [19].

To refine the spectroscopy of ^{13}C above the α-disintegration threshold, we perform, for the first time, a comprehensive R-matrix calculation of several reaction channels involving the structure of ^{13}C as a compound system. A comprehensive analysis is required because of the extremely complex structure of this nucleus. The data sets included in our calculations are: (1) elastic scattering (α_0) differential cross sections (DCS) obtained at several backward angles and previously published in our previous investigation [103], (2) inelastic scattering DCS to the first excited state (α_1, corresponding to $E_x = 1.684$ MeV) in ^{9}Be obtained at $\theta_{\rm lab} = 70°$ extracted from the data of Ref. [103] with the procedure described in Refs. [83,104], and (3) integrated cross sections of ^{9}Be(α,n$_0$)^{12}C and ^{9}Be(α,n$_1$)^{12}C (associated to the residual ^{12}C in the 4.44 MeV state) reactions from Refs. [105,106] and, to complement the low energy part of data, (4) the elastic DCS data at $\theta_{\rm cm} = 160°$,150° taken from Ref. [89] and covering the energy range $E_\alpha \simeq$ 1.0–1.7 MeV. To account for possible normalization errors in the

old data of Ref. [89], we allowed the presence of normalization factors (within ±15%) in our R-matrix procedure. Additionally, to match the two datasets from Refs. [105,106] at low energies, we normalized the n_1 data of Ref. [106] by a 0.52 factor; it is indeed reasonable to assume the possible presence of absolute normalization error in these very old data sets involving the detection of neutrons. To simultaneously fit the data sets described above, we used the multi-channel, multi-level R-matrix code AZURE2 [67,68]. The maximum order of partial waves contributing to the reaction or scattering events was set to $\ell = 8$. The channel radii used in the R-matrix calculation are computed in analogy to the ^{11}C case described in Sect. 3.1 of this paper. The starting parameters of our fit were set by using the ones suggested by the table of states reported in Ref. [35], updated with the more recent findings described in Ref. [15]. The presence of several angles and several reaction channels, including neutron emission channels, is crucial as it allows us to accurately discriminate between contrasting J^π assignments reported in the literature. For clarity reasons, we do not report here the complete spectroscopy of ^{13}C obtained with our study; this can be found in Refs. [83,104]. We will limit here to a discussion regarding the details of our fit procedure and the influence of our results on the appearance of ^{13}C cluster states.

Figure 10 shows the results of our comprehensive R-matrix fit, obtained with a simultaneous fit procedure of the above discussed data sets, for the ^{9}Be(α,α)^{9}Be DCS data at $\theta_{\rm LAB} = 110°$, $\theta_{\rm LAB} = 135°$, $\theta_{\rm LAB} = 150°$, $\theta_{\rm LAB} = 160°$ of Ref. [60]. As clearly visible, the quality of the fit is satisfactory for all the excitation functions. Depending on the reaction channel, the reduced χ^2 goes from ≈ 0.6 up to ≈ 2 for all the data sets used in the fit procedure, as described in detail in Ref. [104]. A detailed description of the fit results follows.

In the $E_{\rm cm} = 1$–2 MeV region, the presence of excited states in ^{13}C leads to the appearance of a marked local minimum in the α_0 channel well-visible in the data of Ref. [89]. Several peaks are also present in the n_0 and n_1 neutron channels of Ref. [105]. The small peak seen at $E_{\rm cm} \simeq 1.11$ MeV in the n_0 excitation function is attributed to the presence of a $3/2^-$ state at 11.75 MeV, already seen in $n+^{12}$C scattering experiment [35]. For this state, the literature reporst a neutron branching ration $\frac{\Gamma_n}{\Gamma_{\rm tot}} = 0.80 \pm 0.08$ and a total width of 129 ± 40 keV [35]. In our work, we obtain $\frac{\Gamma_{n_0}}{\Gamma_{\rm tot}} = 0.97$ and $\Gamma_{\rm tot} = 116$ keV, in quite good agreement with the reported ones. The n_0 and n_1 cross sections show a marked maximum at $E_{\rm cm} \simeq 1.33$ MeV, while the elastic channel shows a dip. In Ref. [89], this dip is attributed to a $5/2^+$ state at 11.97 MeV. This is in excellent agreement with our findings. For this state, we report $\frac{\Gamma_n}{\Gamma_{\rm tot}} \approx 0.57$, also in good agreement with the one quoted by the literature (0.51 ± 0.06, [35]). Also the width (152 keV) and the Γ_α partial width (65 keV) are in good agreement with the findings of Ref. [89]. In the n_0 data, a bump is reported at $E_{\rm cm} \simeq 1.53$ MeV; we attribute this feature to a $5/2^-$ state at 12.17 MeV. In the literature, a group of 4 close-lying states is reported in this energy region [35]. One of those (12.13 MeV, $5/2^-$) could be the candidate for our $5/2^-$. For this state, Wheldon and collaborators reported $\Gamma_{\rm tot} = 219$ keV and $\frac{\Gamma_n}{\Gamma_{\rm tot}} \approx 1$ [99], in agreement with our findings. We introduce a $1/2^+$ excited state at 12.33 MeV, with non-vanishing α and n_0 widths, to reproduce the shoulder well-visible in the n_0 data at $E_{\rm cm} \simeq 1.79$ MeV. At 12.45 MeV, we include a $7/2^-$ state, responsible for the bump in the ^{9}Be(α,n$_1$)^{12}C$_{4.44}$ excitation function at $E_{\rm cm} \simeq 1.83$ MeV (see [104]). This state is possibly in agreement with the $7/2^-$ state at 12.43 MeV previously suggested in the literature [35].

The $E_{\rm cm} = 2$–3 MeV energy domain is mainly dominated by structureless shapes both in the elastic ([88]) and neutron cross sections. We included a broad $3/2^-$ 13.05 MeV state to reproduce the hole in the n_0 cross section around $E_{\rm cm} \approx 2.6$ MeV and to explain the

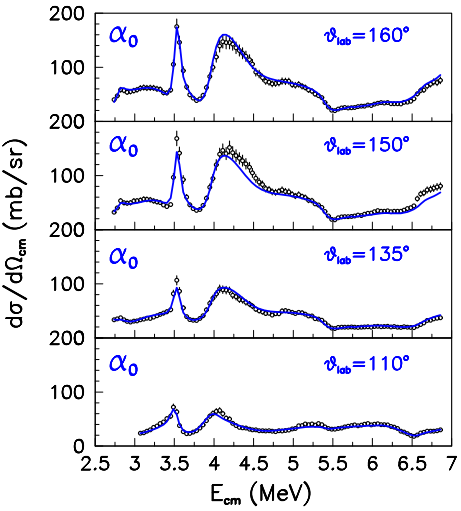

Fig. 9 Simultaneous R-matrix fit (blue lines) of all data sets described in the text shown for the ^{9}Be(α,α)^{9}Be DCS data at $\theta_{\mathrm{LAB}} = 110°$, $\theta_{\mathrm{LAB}} = 135°$, $\theta_{\mathrm{LAB}} = 150°$, $\theta_{\mathrm{LAB}} = 160°$ of Ref. [60]

corresponding shoulder in the n_1 channel at similar energies. This is in agreement with the suggestions of Refs. [15,88], but we quote a larger width (548 keV) than the one determined in previous works. At $E_{\mathrm{cm}} \simeq 2.76$ MeV, we can observe a peculiar shape both in the α_0 and n_1 excitation functions. This was attributed to a tentative $9/2^-$ state at 13.41 MeV ($\Gamma_{\mathrm{tot}} = 58$ keV). More recently, Freer et al. suggested a tentative $7/2^+$ assignment for this state. We can improve this assignment by using a wider angular range in our R-matrix analysis. We succeed in reproducing the shape of our data by using a $9/2^-$ state at 13.41 MeV, having $\Gamma_{\mathrm{tot}} = 84$ keV, and branching ratios $\frac{\Gamma_{\alpha 0}}{\Gamma_{\mathrm{tot}}} \approx 0.25$, $\frac{\Gamma_{n0}}{\Gamma_{\mathrm{tot}}} \approx 0.29$, $\frac{\Gamma_{n1}}{\Gamma_{\mathrm{tot}}} \approx 0.46$. This agrees with the findings reported in Ref. [88]. With our high-quality data; we are therefore able to rule out possible $7/2^+$ assignments for this state; a more detailed discussion on this point is reported in our recent publication [104].

A broad bump is seen in the $\alpha + ^9$ Be elastic scattering data at $E_{\mathrm{cm}} \simeq 2.9$–$3.4$ MeV. At $E_{\mathrm{cm}} \simeq 3.5$ MeV one can see a narrower peak, while a broad local minimum is observed at ($E_{\mathrm{cm}} \simeq 3.85$ MeV), see Fig. 9. The broad bump has a clear evolution with the angle. This interesting feature allows us to determine J^π values contributing in this region. We introduce a couple of broad states at 13.55 MeV ($7/2^-$) and 13.64 MeV ($5/2^+$) to simultaneously reproduce α_0, n_0, and n_1 data in this region. This is in agreement with the findings of Ref. [15]. Following the suggestions by Goss et al [88], we reproduce the peak at $E_{\mathrm{cm}} \simeq 3.5$ MeV in the α_0 data by including two close-lying states at 14.13 MeV ($5/2^-$) and 14.17 MeV ($7/2^+$). The partial widths of the $5/2^-$ state are in good agreement with the previously reported values in Refs. [15,88]. For the $7/2^+$ state, not reported by the authors of Ref. [15], we find a total width much smaller that the one suggested in Ref [88]. A local minimum at $E_{\mathrm{cm}} \simeq 3.85$ MeV, seen in the α_0 DCS data at all angles is due to the interference of a $7/2^-$ state at 14.27 MeV with the neighboring states and the Coulomb background amplitudes. Our value ($\Gamma_{\mathrm{tot}} = 392$ keV) agrees with the one quoted in Ref. [35] ($\Gamma_{\mathrm{tot}} = 280 \pm 70$ keV) within two standard deviations.

In the $E_{\mathrm{cm}} = 3.75$–5.5 MeV region, we identify some broad structures in the neutron emission channels. To describe this trend, we used four states at 14.36 MeV ($9/2^+$), 14.64 MeV ($7/2^-$), 15.04 MeV ($5/2^+$) and 15.27 MeV ($3/2^+$). The interference of the last two of

these states is responsible for the bump seen in the elastic DCS data in the $E_{cm} \approx 4.7$–5.4 MeV region.

The $E_{cm} = 5.5$–6.8 MeV region is characterize by a quite smooth behavior in the α_0 DCS data. Two pronounced dips at $E_{cm} \simeq 5.52$ MeV and $E_{cm} \simeq 6.5$ MeV are visible. In this high-energy region, the spectroscopy of ^{13}C reported in the literature is particularly poor [35]. The dip at $E_{cm} \simeq 5.52$ MeV is due to the 16.09 MeV $3/2^+$ state. The presence of a state at $E_x \simeq 16.1$ MeV with Γ_{tot} of the order of 200–300 keV is reported in the literature. We attribute the deep minimum, seen in the α_0 channel at $\theta_{lab} = 110°$ at $E_{cm} \simeq 6.51$ MeV to the interference between two close-lying states at 17.23 ($3/2^+$) and 17.24 ($3/2^-$) MeV. The wing at $E_{cm} \simeq 5.8$ MeV in the α_1 inelastic channel can be attributed to a narrow $5/2^+$ state at 16.40 MeV. Additional four broad states ($\Gamma_{tot} > 1$ MeV) are needed to reproduce the trend of the α_0 and α_1 excitation functions in this region; however, the relevance of our findings in the highest energy region explored by the α_0 DCS data is limited by the absence of firm higher excitation energy data. New experiments in this complicated energy region are highly required.

3.4 ^{16}C

The last nucleus explored in our investigation is the neutron-rich ^{16}C isotope. Following the suggestions of theoretical models, it is crucial to identify excited states in this nucleus decaying through cluster disintegration channels, e.g., ^{10}Be+^{6}He and ^{12}Be+^{4}He [36]. They are possibly linked to the formation of linear chain or triangular configurations of 3α-particles with 4 valence neutrons. Only a small fraction of these states have been potentially identified experimentally, therefore new investigations are needed to understand the clustering nature of this isotope, especially close to the ^{4}He +^{12}Be (13.808 MeV) and ^{6}He +^{10}Be (16.505 MeV) thresholds. In this framework, we investigate the formation and decay of cluster states in ^{16}C by exploiting sequential breakup reactions with radioactive ion beams. These reaction consist in the population of an excited state in the projectile nucleus by means of the interaction with a target and the subsequent disintegration of the excited state via particle emission (more details regarding this technique can be found for example in Refs. [83,107–109]).

Our experiment was carried out at the FRIBs facility of the INFN-LNS. A primary 55 MeV/nucleon ^{18}O beam was accelerated by the LNS K-800 Superconducting Cyclotron on a ^{9}Be 1.5 mm thick production target. A secondary beam constituted by the products of the fragmentation of the primary beam was delivered to the experimental hall by using a fragment-recoil separator with a magnetic rigidity $B\rho \approx 2.8$ Tm and a momentum acceptance $\Delta p/p \approx 0.01$. The resulting secondary beam is a cocktail of various neutron-rich beams mainly constituted by ^{16}C at 49.5 MeV/u ($\approx 10^5$ particles per second), ^{13}B ($\approx 5 \times 10^4$ particles per second) and ^{10}Be at 56 MeV/u ($\approx 4 \times 10^4$ particles per second). Along the beam line, a tagging system (described in Ref. [110]) was installed to identify, particle-by-particle, the beam content. It is constituted by a Micro Channel Plate (MCP) detector followed (at a distance of about 13 m) by a 140μm thick DSSSD. This detection system is capable to measure the energy loss (ΔE DSSSD) of each individual beam particle of the secondary beam through the DSSSD and their time of flight (TOF) between the MCP and the DSSSD. Figure 10 shows the ΔE DSSSD-TOF correlation obtained during the experiment. A series of well-separated bumps are clearly observed, testifying the good capabilities of this technique in identifying beam particles with an extremely low contamination. Ions are identified by the comparison with a beam transport simulation. Labels in figure indicate the identified ions. The ^{16}C is the most abundant beam species and is also well-separated from neighbor nuclei contributions. To date, this is to our knowledge the most intense ^{16}C beams available in a

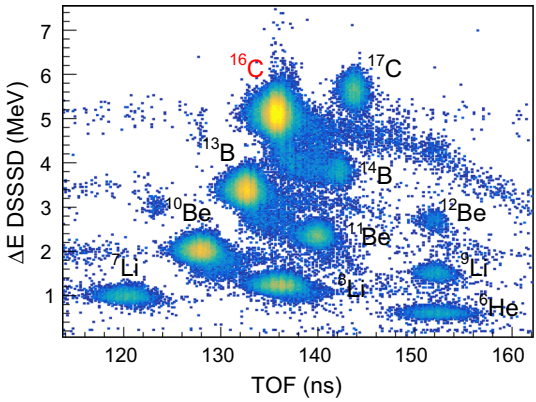

Fig. 10 ΔE DSSSD-TOF correlation produced by means of the tagging system. The TOF is obtained along a ≈ 13 m flying path. Individual nuclear species in the cocktail beam, identified by comparison with beam transport codes, are identified by labels

nuclear physics facility. The information on the impact position on the surface of the DSSSD is used to determine the impinging position on the target. The beam spot size on the target was of the order of 1.5×1.5 cm^2 with a maximum angular spread of 1°. A 50 μm polyethylene $(CH_2)_n$ target was installed in the CHIMERA vacuum chamber to induce projectile breakup reactions. Particles and fragments emitted from the resulting collisions were identified and tracked by means of the 4π detector CHIMERA [111–114]. It consists of 1192 individual Si-CsI(Tl) telescopes, covering $\simeq 94\%$ of the whole solid angle. They are arranged in rings, each of those with a full azimuthal angle coverage and with a variable number of telescopes depending on the θ_{LAB} angle. In our investigation, because of the expected forward focused kinematics of projectile breakup reactions at intermediate energies [107], we use exclusively the first three forward rings of the detector, covering the polar angle range $2.2° \leq \theta \leq 6.4°$, with a reasonable granularity for this experiment (solid angles covered by a single module vary from 0.133 to 0.458 msr at increasing polar angles). Each Si-CsI(Tl) telescope is a two-detection stage detector with a 300 μm thick silicon detector followed by a CsI(Tl) crystal, with thickness ranging from 6 to 12 cm, depending on the angular position in the detector, read-out by a photodiode. Si and CsI(Tl) detectors of the CHIMERA array were calibrated by using elastic scattering of various light ion beams impinging on a polyethylene target. The CsI(Tl) calibrations were performed individually for each incident ion species as described in Ref. [115], by using the calibration formula suggested in Ref. [116]. This is required in order to account for the well-known mass and charge dependence of the light response in inorganic scintillators (see for example Refs. [117,118]). The identification in mass and charge of the detected fragments was based on the $\Delta E - E$ technique. A good isotopic identification is obtained for light ions till beryllium. Heavier fragments, not used in this study, were only identified in charge.

If we assume that a resonant state of the projectile is produced in the intermediate stage of the collision, one can investigate the excitation energy of the nucleus before decaying into fragments by using the invariant mass techniques. In a two-body disintegration, this concept is equivalent to the relative energy between particle E_{rel} [119], which corresponds to the sum of the kinetic energies of the two fragments in their emission center of mass frame. If one uses this formalism, the excitation energy can be calculated as $E_x = E_{rel} + E_{thr}$, where E_{thr} is the particle emission threshold of that particular decay channel. To test the capabilities of our apparatus, we have constructed particle-particle and multi-particle correlations involving α-particles, i.e., the α–α and 3α ones. These are capable to reveal the structure, respectively, of the emitting ^{8}Be and ^{12}C nuclei. Results of this analysis are shown in Fig. 11. The α–α

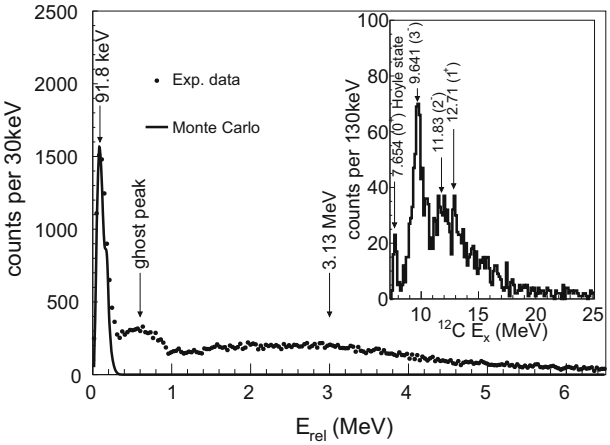

Fig. 11 α–α relative energy investigated with the CHIMERA detector. Peaks reflect the structure of the emitting ^{8}Be nucleus. The result of a Monte Carlo simulation of the 2α emission from the ground state of ^{8}Be is also shown. (insert) ^{12}C excited states reconstructed from 3α-particle invariant mass. States in ^{12}C are well identified

correlation, main panel, shows three distinct features: a pronounced peak at about 90 keV α–α relative energy, a bump at about 600 keV and a broad peak at higher energies. The first is associated, as testified by the result of our complete Monte Carlo simulation, to the 2α-particle emission from the ground state of ^{8}Be. In our Monte Carlo simulation we take into account the beam directions as measured with our DSSSD, the finite size of the target and the detection apparatus, as described more in detail in Refs. [83,120]. We attribute the second bump to the so-called ghost peak of ^{9}Be, in analogy with the observations of Ref. [121]. It is due to the decay by neutron emission of the ^{9}Be 2.43 MeV $5/2^{-}$ state in the low energy tail of the 3.04 MeV 2^{+} state of 8Be. The latter is probably associated to the broad bump at about 3 MeV $E_{\rm rel}$ of Fig. 11. The observed energy shift is probably caused by the drop in efficiency of our detector at high values of relative energy. The insert of Fig. 11 shows the ^{12}C excitation energy spectrum obtained from the 3α-particle invariant mass. Here the Hoyle state, together with few other states in ^{12}C, namely the 9.64 (3^{-}), 11.83 (2^{-}) and 12.71 (1^{-}) MeV states, is clearly observed with an extremely low background level. All these findings clearly testify the consistency of our analysis and the capabilities of the CHIMERA device to reconstruct the spectroscopy of the emitting nucleus via invariant mass studies.

To identify possible ^{16}C decays of excited states above the ^{6}He emission threshold (16.505 MeV) populated in the collisions, we inspected ^{6}He–^{10}Be correlations with the method described above. In this case, because of the limited beam intensity and because of the expected predominant decay mode via neutron emission of this nucleus, the statistics is extremely limited if compared to the one observed for self-conjugate nuclei (Fig. 11). The corresponding result is shown in Fig. 12 in terms of $E_{\rm rel} + E_{\rm thr}$. A non-vanishing yield is recorded at high excitation energies (about 20 MeV). This could represent the possible evidence for a new unreported state in ^{16}C. Interestingly, if one looks at the state-of-the-art ^{16}C investigations via the ^{6}He–^{10}Be channel previously reported in the literature (see the two inserts of Fig. 12 adapted from Refs. [38,39]), a non-vanishing yield is also reported at the same excitation energy, but with a much lower statistics than our investigation. It is interesting to evaluate if such a non-vanishing yield might be attributed to some efficiency effects of our detector or if it could be the evidence of some physics processes, possibly involving the

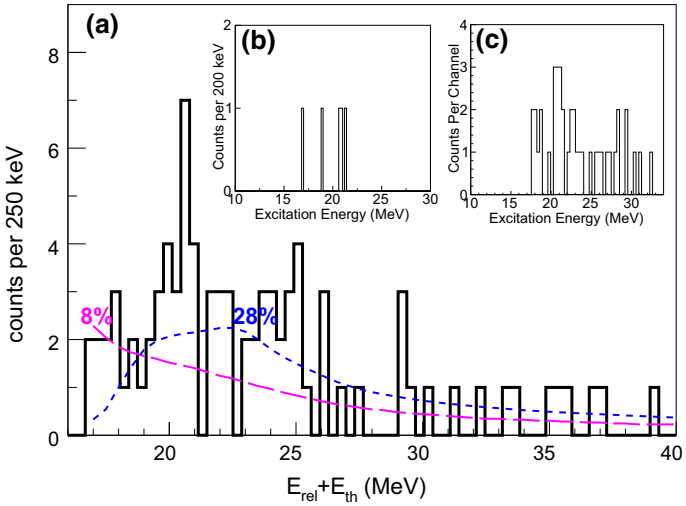

Fig. 12 **a** ^{16}C excitation energy spectrum $E_{\rm rel} + E_{\rm thr}$ obtained via the ^{6}He–^{10}Be correlations. The purple and blue dashed lines are the result of a complete Monte Carlo simulation (see text for details) considering, respectively, that the breakup is induced by carbon or hydrogen recoil. **b**, **c** Analogous results previously published in Ref. [38] (**b**) and in Ref. [39] (**c**)

disintegration into constituent clusters of ^{16}C. To address this point, we have performed a detailed Monte Carlo simulation. We considered the excitation of a ^{16}C beam nucleus on one of the two target components (C or H). As the angular distribution, as suggested in Ref. [107], we used an exponential functional form. In the simulation, we also take into account the energy, angular and position spread of the beam and the geometry of our detector. Results for the two target components are shown with the purple and blue dashed lines, respectively, for breakup events induced by carbon or hydrogen recoil. They have a smooth trend, with maximum values, respectively, 8% and 28%. Such a smooth behavior allows us to conclude that the bump at about 20 MeV observed in the ^{6}He–^{10}Be coincidence spectrum cannot be attributed to efficiency effects. It is clear that the extremely limited statistics does not allow to link such feature to the existence of a state in ^{16}C, as it is also compatible with a phase space decay with non-resonant behavior. However, this finding might serve as a starting point to develop future investigations aimed to investigate the cluster structure of ^{16}C above helium emission threshold.

4 Discussion on rotational bands in ^{11}C and ^{13}C

It is interesting to discuss the contribution of the refined ^{11,13}C spectroscopy on the understanding of their rotational bands.

In addition to the two positive parity bands in ^{11}C suggested in Ref. [40], the authors of Ref. [44] proposed the appearance of a new negative parity rotational band ($K^{\pi} = 3/2^{-}$) in ^{11}C, having the 8.10 MeV state ($3/2^{-}$) as the band head, associated to a 2α-^{3}He configuration. The second member of this band is suggested to be the 9.78 MeV $5/2^{-}$ state. The subsequent member ($7/2^{-}$) is indicated to lie at 11.03 MeV, as shown by their R-matrix fit. Their systematic predicts even a further $9/2^{-}$ member which could be located at around 13 MeV. The latter is only tentatively assigned. In Ref. [44], two states are proposed as candidates for

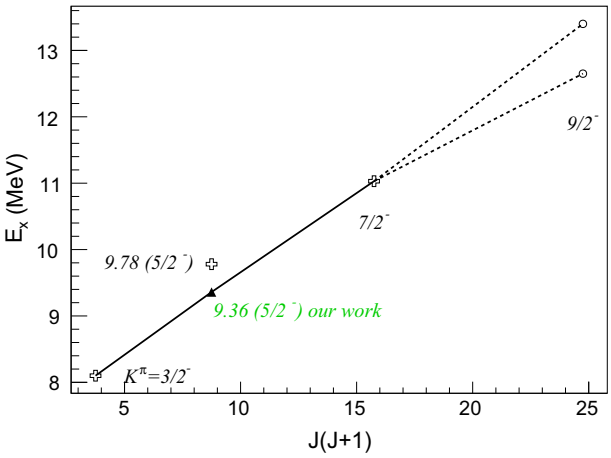

Fig. 13 $K^\pi = 3/2^-$ negative parity rotational band proposed in Ref. [44] (open crosses). Two possible candidates for the $9/2^-$ are also proposed by the authors or Ref. [44] (open dots). The black filled triangle is the 9.36 MeV ($5/2^-$) indicated in this work

the $9/2^-$ of the $K^\pi = 3/2^-$ band in ^{11}C: the 12.65 MeV or the 13.4 MeV state. The situation is described in Fig. 13, where the open crosses represent the states indicated in the systematics of Ref. [44] for the $K^\pi = 3/2^-$ band, and the open dots are the possible candidates for the $9/2^-$ member of this band. If we include in the systematics the state at 9.36 MeV ($5/2^-$) indicated in this work (black filled triangle), we obtain an excellent linear correlation if one considers the 13.4 MeV state as the $9/2^-$ missing member. Giving the pronounced α-nature of the 9.36 MeV state, one can naively speculate that this state could be the $5/2^-$ member of such a molecular rotational band. This interesting speculation could be extremely important if confirmed by future high-precision experiments in this energy region.

A negative parity band in ^{13}C ($K^\pi = 3/2^-$) is proposed in Ref. [19], having the $3/2^-$ and $5/2^-$ members respectively at 9.897 MeV and 10.818 MeV. In our refined spectroscopy scheme, we identify the $7/2^-$ state of this band at 12.45 MeV. For this state, we found a relatively small value of the dimensionless reduced α width $\theta_\alpha^2 \approx 0.05$. Concerning the 14.13 MeV state, we discard the possibility, suggested in Ref. [19], to be a $9/2^-$ state. The $5/2^-$ assignment here reported, in agreement with Refs. [15,88], appears to be very solid. We report instead a $9/2^-$ state at 13.41 MeV. This state has a sizable dimensionless reduced α width ($\theta_\alpha^2 = 0.26$), and we could suppose that it belongs to the $K^\pi = 3/2^-$ band described in Ref. [19]. If we consider the 9.897 MeV and 10.818 MeV states from Ref. [19] and the two additional members obtained with our analysis (12.45 MeV, $7/2^-$ and 13.41, $9/2^-$), as shown in Fig. 14, we observe a reasonable fulfillment of the rotational band rule $E_x = \frac{\hbar^2 J(J+1)}{2\Im} + \text{const}$. If this hypothesis is true, such a molecular band will have a slope coefficient $\frac{\hbar^2}{2\Im} \simeq 171$ keV. This value is very close to the one ($\frac{\hbar^2}{2\Im} \simeq 163$ keV) that can be extracted by a linear fit of theoretical data related to the $K^\pi = 3/2_2^-$ molecular band of Ref. [31]. According to the considerations of Ref. [31], such a large value of moment of inertia might be related to an obtuse triangle configuration of 3α-particles with a valence neutron. Finally, we do not find evidence for the $J^\pi = 11/2^-$ conjectured in Ref. [19].

For the positive parity $K^\pi = 3/2^+$ band proposed in Ref. [19], we identify only the $5/2^+$ level at 11.97 MeV. This state seems to have a pronounced cluster nature, being its reduced

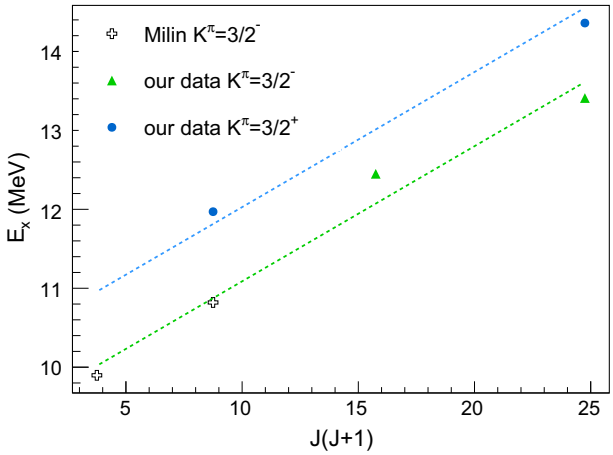

Fig. 14 Positive and negative parity bands in ^{13}C as the result of our refined spectroscopy. The open crosses are the $3/2^-$ and $5/2^-$ members suggested in Ref. [19]. Solid symbols are discussed in the text

α-width a consistent fraction of the Wigner limit ($\theta_\alpha^2 = 0.27$). We also observe a $9/2^+$ state ($\theta_\alpha^2 \approx 0.1$) lying at an excitation energy of 14.36 MeV. If we assume that both states belong to a positive parity band, as shown in Fig. 14, a slope parameter $\frac{\hbar^2}{2\Im} \simeq 150$ keV is found, similar to the one reported for the negative parity band. According to this naive hypothesis, we predict the missing $7/2^+$ member at around 13 MeV, corresponding to $E_{\rm cm} \approx 2.35$ MeV.

5 Summary

Clustering phenomena in carbon isotopes are key to understand the structure of light nuclei and the appearance of molecular-like symmetries in nuclei. To shed light on these aspects, we have developed an experimental campaign to investigate cluster structures in ^{11}C, ^{12}C, ^{13}C, ^{16}C. We use several experimental approaches that involve compound nucleus reactions and direct reactions with the reconstruction of the in-flight resonant decay from the clustered nucleus.

The ^{10}B(p,α)^{7}Be reaction is investigated at $E_p = 0.63$–1.028 MeV to populate ^{11}C states above p-threshold. We adopt the technique of the inverse absorber to overcome previous limitations, arising from the presence of contaminant reactions, that prevented firm direct investigations in this energy region. We perform a comprehensive R-matrix analysis of our new data, complemented with previously published data involving the structure of ^{11}C. In our new refined spectroscopy scheme, we clearly identify a new cluster state at $E_x = 9.36$ ($5/2^-$). This state could be associated to a 2α-^{3}He configuration and be the $5/2^-$ of the $K^\pi = 3/2^-$ rotational band.

We investigate the possible existence of direct decays from the Hoyle state (7.654 MeV, 0^+) in ^{12}C. To reach an unprecedented level of precision, we develop a high-precision and high-selectivity experiment using the ^{14}N(d,α)^{12}C reaction at 10.5 MeV. ^{12}C* decays from the Hoyle state are identified by means of a new-generation hodoscope of silicon detectors. We obtain a new upper limit of the direct decay branch of this state of 0.043% of the sequential one, improving of a factor of 5 the previous state-of-the-art limit.

The spectroscopy of ^{13}C is investigated in a broad energy domain ($E_x > 10.648$ MeV) by performing a comprehensive R-matrix analysis of several $\alpha+^{9}$Be reactions. We significantly refine the ^{13}C spectroscopy, solving several ambiguities present in the literature regarding position and J^{π} assignment of excited states. We suggest the possible appearance of exotic molecular configuration by linking our states to previously suggested ^{13}C rotational bands.

Finally, we investigate the ^{16}C nucleus by using a fragmentation cocktail beam and sequential breakup reactions induced by a polyethylene target. We identify possible ^{6}He–^{10}Be decays of high-lying states in ^{16}C, suggesting the possible presence of a new unreported state in ^{16}C at about 20 MeV excitation energy.

Acknowledgements I want also to acknowledge the staff of the tandem accelerator of Naples, the tandem accelerator of INFN-LNS and the K-800 cyclotron of INFN-LNS (FRIBs facility) for having delivered high-quality beams. I am indebted to Dr. Miguel Marques (LPC Caen) for useful discussions and for his careful review of the contents discussed in the paper.

References

1. J.A. Wheeler, Phys. Rev. **52**, 1107 (1937)
2. L.R. Hafstad, E. Teller, Phys. Rev. **54**, 681 (1938)
3. W. von Oertzen, Z. Phys. A **354**, 37 (1996)
4. N. Itagaki, S. Okabe, K. Ikeda, Phys. Rev. C **62**, 034301 (2000)
5. Y. Kanada-En'yo, H. Horiuchi, Phys. Rev. C **68**, 104319 (2003)
6. N. Itagaki, S. Okabe, K. Ikeda, I. Tanihata, Phys. Rev. C **64**, 014301 (2001)
7. N. Itagaki, S. Okabe, Phys. Rev. C **61**, 044306 (2000)
8. M. Seya, M. Kohno, S. Nagata, Prog. Theor. Phys. **65**, 206 (1981)
9. M. Freer, Rep. Prog. Phys. **70**, 2149 (2007)
10. Y. Kanada-En'yo, H. Horiuchi, A. Doté, J. Phys. G Nucl. Part. Phys. **24**, 1499 (1998)
11. M. Freer et al., Phys. Rev. Lett. **96**, 042501 (2006)
12. Z.H. Yang et al., Phys. Rev. C **91**, 024304 (2015)
13. D. Suzuki et al., Phys. Rev. C **87**, 054301 (2013)
14. W. von Oertzen, Z. Phys. A **357**, 355 (1997)
15. M. Freer, Phys. Rev. C **84**, 034317 (2011)
16. M. Freer et al., Rev. Mod. Phys. **90**, 035004 (2018)
17. N. Soić et al., Phys. Rev. C **68**, 014321 (2003)
18. M. Milin et al., Nucl. Phys. A **730**, 285 (2004)
19. M. Milin, W. von Oertzen, Eur. Phys. J. A **14**, 295 (2002)
20. T. Suhara, Y. Kanada-En'yo, Phys. Rev. C **84**, 024328 (2011)
21. T. Suhara, Y. Kanada-En'yo, Phys. Rev. C **82**, 044301 (2010)
22. W. von Oertzen et al., Eur. Phys. J. A **21**, 193 (2004)
23. K. Ikeda et al., Prog. Theor. Phys. Suppl. E **68**, 464 (1968)
24. H. Morinaga, Phys. Rev. **101**, 254 (1956)
25. M. Itoh et al., Phys. Rev. C **84**, 054308 (2011)
26. M. Freer, Phys. Rev. C **86**, 034320 (2012)
27. S. Ishikawa, Phys. Rev. C **90**, 061604(R) (2014)
28. E. Epelbaum et al., Phys. Rev. Lett. **109**, 252501 (2012)
29. M. Freer, Prog. Part. Nucl. Phys. **78**, 1 (2014)
30. T. Yoshida, N. Itagaki, T. Otsuka, Phys. Rev. C **79**, 034308 (2009)
31. N. Furutachi, M. Kimura, Phys. Rev. C **83**, 021303 (2011)
32. Y. Chiba, M. Kimura, J. Phys. Conf. Ser. **569**, 012047 (2014)
33. T. Yamada, Y. Funaki, Phys. Rev. **92**, 034326 (2015)
34. M. Freer, Phys. Rev. C **85**, 014304 (2012)
35. F. Ajzenberg-Selove, Nucl. Phys. A **523**, 1 (1991)
36. T. Baba, Y. Chiba, M. Kimura, Phys. Rev. **90**, 064319 (2004)
37. D.R. Tilley et al., Nucl. Phys. A **564**, 1 (1993)
38. P.J. Leask et al., J. Phys. G Nucl. Part. Phys. **27**, B9 (2001)
39. N.I. Ashwood et al., Phys. Rev. C **70**, 064607 (2004)

40. N. Soić et al., Nucl. Phys. A **742**, 271 (2004)
41. Y. Kanada-En'yo, Phys. Rev. C **75**, 024302 (2007)
42. T. Kawabata et al., Phys. Rev. C **70**, 034318 (2004)
43. T. Kawabata et al., Phys. Lett. B **646**, 6 (2007)
44. H. Yamaguchi et al., Phys. Rev. C **87**, 034303 (2013)
45. M. Wiescher et al., Phys. Rev. C **28**, 1431 (1983)
46. C. Spitaleri et al., Phys. Rev. C **95**, 035801 (2017)
47. A.M. Boesgard et al., Astrophys. J. **621**, 991 (2005)
48. R.J. Peterson et al., Ann. Nucl. Energy **2**, 503 (1975)
49. M.C. Spraker et al., J. Fusion Energy **231**, 357 (2012)
50. I. Lombardo et al., J. Phys. G Nucl. Part. Phys. **43**, 045109 (2016)
51. J.W. Cronin et al., Phys. Rev. **101**, 298 (1956)
52. G. Baur et al., Nucl. Phys. A **458**, 188 (1986)
53. C. Spitaleri et al., Phys. Rev. C **60**, 055802 (1999)
54. M. La Cognata et al., Astrophys. J. **805**, 128 (2015)
55. J.G. Jenkin et al., Nucl. Phys. A **50**, 516 (1964)
56. A. Kafkarkou et al., Nucl. Instrum. Meth. Phys. Res. B **316**, 48 (2013)
57. N.A. Roughton et al., At. Data Nucl. Data Tables **23**, 177 (1979)
58. A.B. Brown et al., Phys. Rev. **82**, 159 (1951)
59. L. Campajola et al., Nucl. Instrum. Meth. Phys. Res. B **29**, 129 (1987)
60. I. Lombardo et al., J. Phys. G Nucl. Part. Phys. **40**, 1251102 (2013)
61. I. Lombardo et al., J. Phys. Conf. Ser. **569**, 012068 (2014)
62. I. Lombardo et al., Bull. Russ. Acad. Sci. Phys. **78**, 1093 (2014)
63. M. Chiari, L. Giuntini, P.A. Mandó, N. Taccetti, Nucl. Instr. Meth. Phys. Res. B **309**, 184 (2001)
64. M. Chiari, L. Giuntini, P.A. Mandó, N. Taccetti, Nucl. Instr. Meth. Phys. Res. B **343**, 70 (2015)
65. J.-J. He et al., Chin. Phys. C **42**, 015001 (2018)
66. J.C. Overley, W. Whaling, Phys. Rev. **128**, 315 (1962)
67. R.E. Azuma et al., Phys. Rev. C **81**, 045805 (2010)
68. R.J. De Boer et al., Phys. Rev. C **91**, 045804 (2015)
69. J.H. Kelley et al., Nucl. Phys. A **880**, 88 (2012)
70. C. Spitaleri et al., Phys. Rev. C **90**, 035801 (2014)
71. O.S. Kirsebom et al., Phys. Rev. Lett. **108**, 202501 (2012)
72. M. Freer, Phys. Rev. C **49**, R1751 (1994)
73. Ad R. Raduta et al., Phys. Lett. B **705**, 65 (2011)
74. J. Manfredi et al., Phys. Rev. C **85**, 037603 (2012)
75. T.K. Rana et al., Phys. Rev. C **88**, 021601(R) (2013)
76. M. Itoh et al., Phys. Rev. Lett. **113**, 102501 (2014)
77. D. Dell'Aquila et al., J. Phys. Conf. Ser. **876**, 012006 (2017)
78. D. Dell'Aquila et al., EPJ Web Conf. **165**, 01020 (2017)
79. D. Dell'Aquila et al., EPJ Web Conf. **184**, 01005 (2018)
80. D. Dell'Aquila et al., Nucl. Instr. Meth. Phys. Res. A **877**, 227 (2018)
81. W. Koenig et al., Il Nuovo Cim. **39**, 9 (1977)
82. D. Dell'Aquila et al., AIP Conf. Proc. **2038**, 020015 (2018)
83. D. Dell'Aquila, Clustering in light nuclear systems: a multi-method approach. PhD thesis, Università degli Studi di Napoli "Federico II" and Univeristé Paris-Sud (Paris-Saclay) (2018)
84. D. Dell'Aquila et al., Phys. Rev. Lett. **119**, 132501 (2017)
85. G.J. Feldman, R.D. Cousins, Phys. Rev. D **57**, 3873 (1998)
86. R.J. Barlow, *Statistics* (Wiley, Chichester, 1989)
87. R.B. Taylor, N.R. Fletcher, R.H. Davis, Nucl. Phys. **65**, 318 (1965)
88. J.D. Goss et al., Phys. Rev. C **7**, 1837 (1973)
89. Z.A. Saleh et al., Ann. der Phys. **7**, 76 (1974)
90. J. Leavitt et al., Nucl. Instrum. Meth. Phys. Res. B **85**, 37 (1994)
91. J. Liu, Z. Zheng, W.K. Chu, Nucl. Instrum. Meth. Phys. Res. B **108**, 247 (1996)
92. M. Zadro et al., Nucl. Instrum. Meth. Phys. Res. B **259**, 836 (2007)
93. A.W. Obst, T.B. Grandy, J.L. Weil, Phys. Rev. C **5**, 738 (1972)
94. D.C. De Martini, C.R. Soltesz, T.R. Donoghue, Phys. Rev. C **7**, 1824 (1973)
95. D.E. Groce, B.D. Sowerby, Nature **206**, 494 (1965)
96. H.D. Knox, R.O. Lane, Nucl. Phys. A **378**, 503 (1982)
97. W. Tornow, J. Phys. G Nucl. Phys. **9**, 1507 (1983)
98. H.E. Hall, T.W. Bonner, Nucl. Phys. **14**, 295 (1959)

99. C. Wheldon et al., Phys. Rev. C **86**, 044328 (2012)
100. X. Aslanoglou et al., Phys. Rev. C **40**, 73 (1989)
101. T. Kawabata et al., J. Phys. Conf. Ser. **111**, 012013 (2008)
102. John M. Blatt, Victor F Weisskopf, *Theoretical Nuclear Physics*, 1st edn. (Wiley, New York, 1962)
103. I. Lombardo et al., Nucl. Instr. Meth. Phys. Res. B **302**, 19 (2013)
104. I. Lombardo et al., Phys. Rev. C **97**, 034320 (2018)
105. R. Kunz et al., Phys. Rev. C **53**, 2486 (1996)
106. L. van der Zwan, K.W. Geiger, Nucl. Phys. A **152**, 481 (1970)
107. M. Freer et al., Phys. Rev. C **63**, 034301 (2001)
108. D. Dell'Aquila et al., CERN-Proceedings **001**, 209 (2015)
109. D. Dell'Aquila et al., EPJ Web Conf. **117**, 06011 (2016)
110. I. Lombardo et al., Nuc. Phys. Proc. Suppl. **215**, 272 (2011)
111. E. De Filippo, A. Pagano, EPJ A **50**, 32 (2014)
112. A. Pagano, Nucl. Phys. News **22**, 25 (2012)
113. I. Lombardo et al., Nucl. Phys. A **834**, 458c (2010)
114. E. De Filippo et al., Acta Phys. Pol. B **40**, 1199 (2009)
115. L. Acosta et al., Nucl. Instr. Meth. Phys. Res. A **715**, 56 (2013)
116. D. Horn et al., Nucl. Instr. Meth. Phys. Res. A **320**, 273 (1992)
117. D. Dell'Aquila et al., Nucl. Instr. Meth. Phys. Res. A **929**, 162 (2019)
118. M. Pârlog et al., Nucl. Instr. Meth. Phys. Res. A **482**, 674 (2002)
119. J. van Driel, Phys. Lett. B **98**, 351 (1981)
120. D. Dell'Aquila et al., Phys. Rev. C **93**, 024611 (2016)
121. S. Ahmed et al., Phys. Rev. C **69**, 024303 (2004)